Sequential localization of a complex electron fluid

Valentina Martelli[a,1,2], Ang Cai[b,c,1], Emilian M. Nica[b,c,3], Mathieu Taupin[a], Andrey Prokofiev[a], Chia-Chuan Liu[b,c], Hsin-Hua Lai[b,c], Rong Yu[b,c,d], Kevin Ingersent[e], Robert Küchler[f], André M. Strydom[g], Diana Geiger[a], Jonathan Haenel[a], Julio Larrea[a,2], Qimiao Si[b,c,4], and Silke Paschen[a,b,c,4]

[a]Institute of Solid State Physics, Vienna University of Technology, 1040 Vienna, Austria; [b]Department of Physics and Astronomy, Rice University, Houston, TX 77005; [c]Rice Center for Quantum Materials, Rice University, Houston, TX 77005; [d]Department of Physics, Renmin University of China, Beijing 100872, China; [e]Department of Physics, University of Florida, Gainesville, FL 32611-8440; [f]Physics of Quantum Materials, Max Planck Institute for Chemical Physics of Solids, 01187 Dresden, Germany; and [g]Highly Correlated Matter Research Group, Physics Department, University of Johannesburg, Auckland Park 2006, South Africa

Edited by Zachary Fisk, University of California, Irvine, CA, and approved July 26, 2019 (received for review May 10, 2019)

Complex and correlated quantum systems with promise for new functionality often involve entwined electronic degrees of freedom. In such materials, highly unusual properties emerge and could be the result of electron localization. Here, a cubic heavy fermion metal governed by spins and orbitals is chosen as a model system for this physics. Its properties are found to originate from surprisingly simple low-energy behavior, with 2 distinct localization transitions driven by a single degree of freedom at a time. This result is unexpected, but we are able to understand it by advancing the notion of sequential destruction of an SU(4) spin–orbital-coupled Kondo entanglement. Our results implicate electron localization as a unified framework for strongly correlated materials and suggest ways to exploit multiple degrees of freedom for quantum engineering.

quantum criticality | spin–orbital entwining | electron localization–delocalization transition | heavy fermion compounds | Kondo destruction

Strongly correlated electron systems represent a vibrant frontier in modern condensed-matter physics. They often contain multiple degrees of freedom, which may be harnessed for future applications in electronic devices. One famous example is the manganites, in which both spin and orbital degrees of freedom play an important role (1). Others are the iron-based superconductors (2) and fullerides (3). In the cuprates, charge order emerges and interplays with the spin degrees of freedom to influence their low-energy properties (4, 5). Even in magic-angle graphene, the physics likely depends on both the spin and valley degrees of freedom (6). These systems display a rich variety of exotic properties at low energies (4–12). Finding simplicity out of this complexity is a central goal of the field. An emerging notion is that electron localization may be an organizing principle that can accomplish this goal (13).

Results

We have chosen heavy fermion materials as a setting for our study because they can be readily tuned to localization transitions and display sharp features thereof. The f electron's spin in a heavy fermion compound corresponds to a well-defined local degree of freedom. At the same time, it is still sufficiently coupled to the conduction electrons that its behavior can be probed through the latter. In the ground state, Kondo entanglement generally leads to the formation of a many-body spin singlet between the local moment and conduction electrons. Electronic localization of this electron fluid can then be realized as a function of a nonthermal control parameter (8–11, 14–18) and has been understood in terms of the destruction of Kondo entanglement (19–22). The accompanying strange-metal behavior, the onset of magnetic ordering of the liberated spins, and unconventional superconductivity are prominent features (8–11, 14–18) that make this transition both readily observable and broadly important.

To explore the intricate interplay of multiple quantum numbers in this setting, a local degree of freedom in addition to the electron's spin should come into play. The simplest such case in heavy fermion systems may arise in cubic Ce-based compounds. Due to strong intraatomic spin–orbit coupling, the spin and orbital degrees of freedom of the Ce $4f^1$ electron are described in terms of the total angular momentum $\boldsymbol{J}$ that encompasses both spins (dipoles) and higher multipolar moments. Ce- and Yb-based heavy fermion materials often have crystalline symmetries lower than cubic. In that case, the lowest crystal electric field (CEF) level would be a Kramers doublet. In the cubic case, however, symmetry allows for CEF levels with higher degeneracy, such as the 4-fold Γ_8 level, in the case of both the $[\mathrm{Xe}]4f^1$ wavefunction of a Ce^{+3} ion (for the total angular momentum $J=5/2$) and the $[\mathrm{Xe}]4f^{13}$ wavefunction of a Yb^{+3} ion (for $J=7/2$). When this level is the lowest in energy, we end up with 1 f electron (or hole in the Yb-based systems) occupying a 4-fold degenerate local level, which can be characterized by spin and orbital quantum numbers (23). This is indeed the case in the intermetallic compound $Ce_3Pd_{20}Si_6$ (Fig. 1*A* and *SI Appendix*, section S4). In zero field, it is at first the quadrupolar moments that order into an antiferroquadrupolar (AFQ) phase

Significance

Many of the most fascinating and actively investigated materials classes host strongly correlated electrons. Their understanding is challenging because the strong correlations cause entwining of multiple degrees of freedom of an electron, such as spin, orbital, and charge. This complexity is ubiquitous and underlies many of the rich properties. The question then is whether there are universal organizing principles that provide simplicity to the description. Here, by studying a prototype material with entwined spin and orbital degrees of freedom and a theoretical model pertinent to it, we have demonstrated correlation-driven electron localization–delocalization as such a principle. It happens sequentially, involving a single quantum number at a time, thus deciphering the roles of the individual degrees of freedom.

Author contributions: Q.S. and S.P. designed research; V.M., A.C., E.M.N., M.T., A.P., C.-C.L., H.-H.L., R.Y., K.I., R.K., A.M.S., D.G., J.H., J.L., Q.S., and S.P. performed research; and Q.S. and S.P. wrote the paper with assistance from A.C.

The authors declare no conflict of interest.

This article is a PNAS Direct Submission.

[1]V.M. and A.C. contributed equally to this work.

[2]Present address: Institute of Physics, University of São Paulo, CEP 05508-090 São Paulo, Brazil.

[3]Present address: Department of Physics and Astronomy and Quantum Matter Institute, University of British Columbia, Vancouver, BC, V6T 1Z1, Canada.

[4]To whom correspondence may be addressed. Email: qmsi@rice.edu or paschen@ifp.tuwien.ac.at.

This article contains supporting information online at www.pnas.org/lookup/suppl/doi:10.1073/pnas.1908101116/-/DCSupplemental.

Published online August 20, 2019.

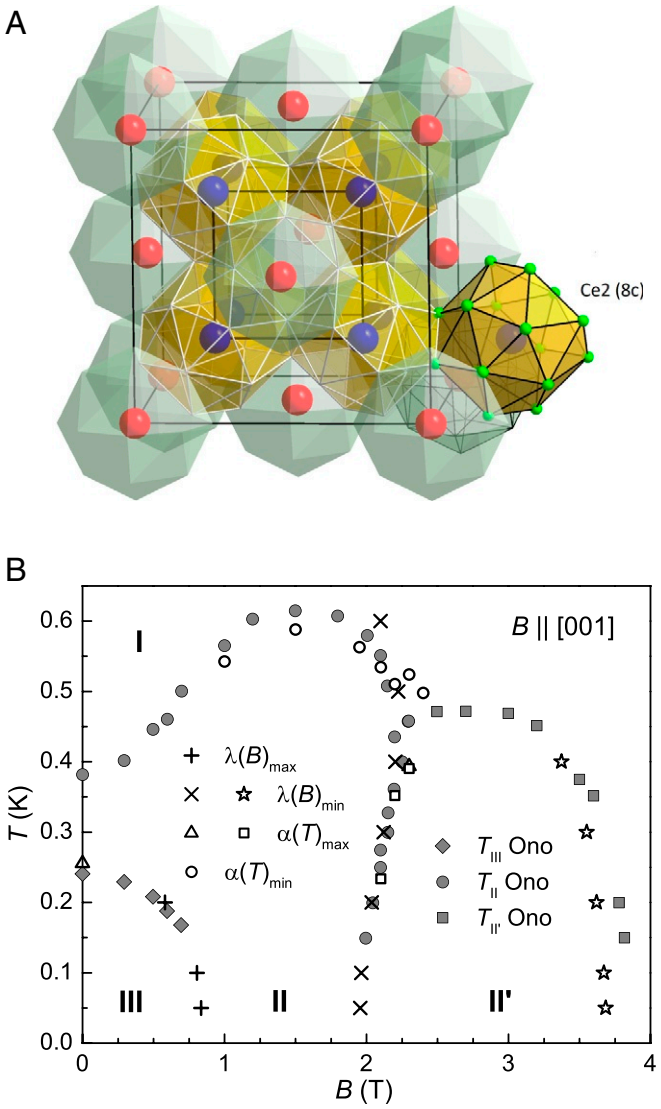

Fig. 1. Crystal structure and ordered phases of the heavy fermion compound $Ce_3Pd_{20}Si_6$. (*A*) Cubic crystal structure of space group $Fm\bar{3}m$ (25) with the 2 Ce sites 4*a* (Ce1, red) and 8*c* (Ce2, blue), both with cubic point symmetry, forming a face-centered cubic lattice of lattice parameter $a = 12.275$ Å (26) and a simple cubic lattice of half the lattice parameter, respectively. The polyhedra around Ce1 are made up of Si and Pd and those around Ce2 of Pd only. This structure persists down to at least 40 mK, as shown by high-resolution neutron diffraction measurements (27). (*B*) Temperature–magnetic-field phase diagram for fields $B = \mu_0 H$ applied along [0 0 1]. The phase boundaries are determined from specific heat data by Ono et al. (28) (T_{III} Ono, T_{II} Ono, and $T_{II'}$ Ono refer to anomalies upon entering phases III, II, and II′, respectively), and our magnetostriction [$\lambda(B)_{max}$ and $\lambda(B)_{min}$ mark the positions of the maxima and minima in $\lambda(B)$ (*SI Appendix*, Fig. S1*B*)] and thermal expansion data [$\alpha(B)_{max}$ and $\alpha(B)_{min}$ mark the positions of the maxima and minima of $\alpha(T)$ (*SI Appendix*, Fig. S1*C*)]. Phase I is paramagnetic, and the order of phases II and III was identified as AFQ and AFM order of moments on the 8*c* cite, respectively; the nature of the order of phase II′ remains to be identified (24). Neutron scattering has not detected any order associated with the 4*a* site (24). Phase III is isotropic with respect to the field direction, but phase II extends to fields above 10 T for fields along [1 1 0] and [1 1 1] (28). Thus, it is advantageous to study $B \| [0\,0\,1]$, as done in the present work.

with ordering wave vector $[1\,1\,1]$ at $T_Q \sim 0.4$ K; with further decreasing temperature, the dipolar (magnetic) moments undergo antiferromagnetic (AFM) ordering, with the ordering wave vector $[0\,0\,0.8]$ at $T_N \sim 0.25$ K, as shown by recent neutron scattering experiments (24). Both orders are due to Ce atoms on the crystallographic $8c$ site.

As typical for heavy fermion systems, the many-body ground state is readily tunable by external parameters such as magnetic field. Previous work on $Ce_3Pd_{20}Si_6$ polycrystals (15) indeed revealed the suppression of T_N at a critical field B_N. Quantum criticality was revealed by electrical resistivity and specific heat measurements; the temperature dependencies were found to be different from the expectations (29) of the conventional theory based on order parameter fluctuations. Measurements of magnetotransport revealed a jump of the Hall coefficient and magnetoresistance in the zero-temperature limit across B_N, which implicates a sudden reconstruction from large to small Fermi surface with decreasing field, as expected for a localization transition of Kondo destruction type (15). When single crystals became available (*SI Appendix*, section S1), the phase diagram was mapped out for different field orientations (28). The AFM transition is suppressed isotropically, implying that the quantum critical behavior at B_N observed in polycrystals captures the behavior of the single crystals. By contrast, the AFQ transition is suppressed anisotropically (24, 28). The study of the interplay between spin and orbital degrees of freedom thus requires measurements on single crystals, which we carry out in the present work.

We chose to apply a magnetic field along the crystallographic $[0\,0\,1]$ direction, which suppresses the AFQ phase at a relatively small field B_Q (*SI Appendix*, section S2). The temperature–magnetic-field phase diagram for this direction is shown in Fig. 1*B*. The AFM phase (phase III) is suppressed at $B_N \sim 0.8$ T, whereas the AFQ phase (phase II) is suppressed at $B_Q \sim 2$ T. Both phase transitions have been found to be continuous by neutron scattering experiments (24). The continuous nature of the transition at B_Q is also evidenced by the phase transition anomalies in specific heat (28), magnetostriction (*SI Appendix*, Fig. S1 *A* and *B*), and thermal expansion data (*SI Appendix*, Fig. S1*C*). The notion (15) that the Fermi surface is large at $B > B_N$ appears to have 2 implications. First, no further jump is to be expected at larger fields. Indeed, it has been taken for granted that electron localization takes place only once even in the case with multiple degrees of freedom. Second, the quantum critical behavior at B_Q should be very different from that near B_N.

Surprisingly, we find strange-metal behavior near B_Q that is strikingly similar to that near B_N, as illustrated by the power-law exponent a of the temperature-dependent electrical resistivity ($\rho = \rho_0 + A' \cdot T^a$) in the quantum critical fans anchored at B_Q and B_N, respectively (Fig. 2*A*). Indeed, at B_Q, the electrical resistivity ρ is linear in temperature down to very low temperatures (Fig. 2*B*), and the specific heat coefficient c/T shows a logarithmic divergence (Fig. 2*C*, right axis). In addition, the thermal expansion coefficient α/T shows a stronger than logarithmic divergence (Fig. 2*C*, left axis), consistent with a diverging Grüneisen parameter $\Gamma \sim \alpha/c$. At fields away from B_Q, Fermi liquid (FL) behavior, with the form $\rho = \rho_0 + A \cdot T^2$, is recovered in the electrical resistivity (Fig. 2*B*, at temperatures below the arrows). The A coefficient, extracted from the respective FL regimes (*SI Appendix*, Fig. S2), is strongly enhanced toward B_N and B_Q (Fig. 2*D*). To further characterize the behavior near B_Q, we have measured the isothermal field dependence of the electrical resistivity (Fig. 3 *A*–*C*) and the Hall resistivity (Fig. 3 *D*–*F*) across this critical field. They reveal cross-over signatures which can be quantified following the procedures established previously (10, 14, 15) (*SI Appendix*, section S3). The characteristic parameters extracted from the analysis at each temperature are the full width at half maximum (FWHM) of the cross-over (Fig. 3*G*), the cross-over height ΔA (Fig. 3*H*), and the cross-over field B^* or, equivalently, the field-dependent cross-over temperature scale T^* (Fig. 4*A*). The pure power-law behavior of the FWHM is seen as a straight line in a double-logarithmic

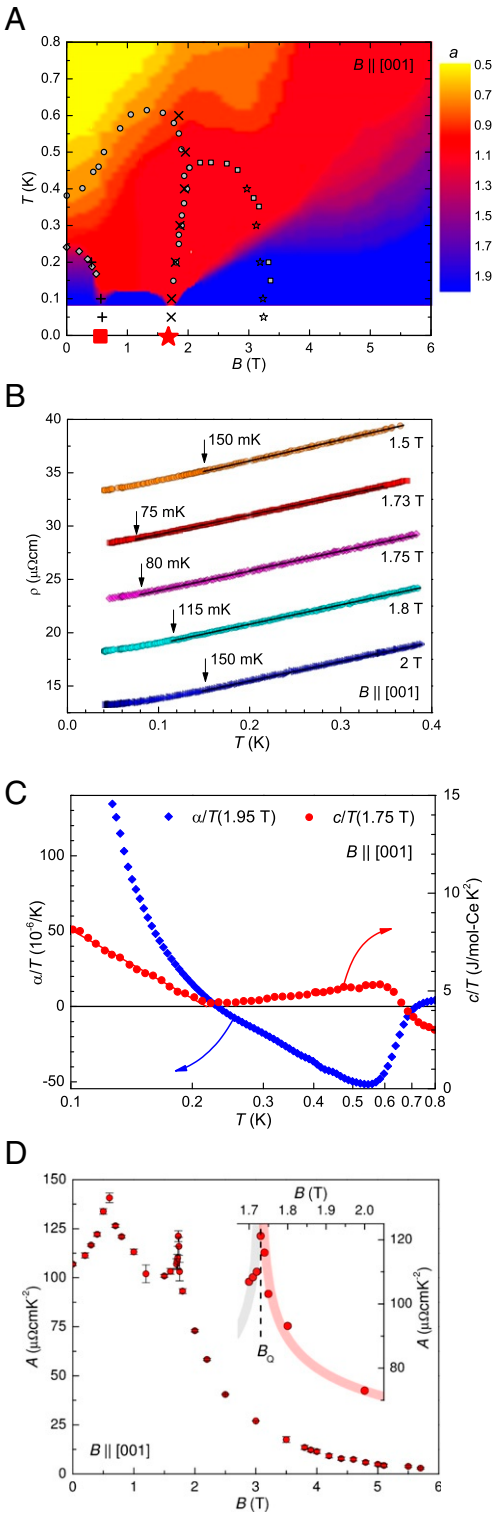

Fig. 2. Signatures of quantum criticality at the border of the AFQ phase in $Ce_3Pd_{20}Si_6$. (*A*) Contour plot of the resistivity exponent a of $\rho = \rho_0 + A' \cdot T^a$ in the temperature–magnetic-field phase diagram for $B = \mu_0 H \| [0\,0\,1]$. To match the critical fields of our electrical resistivity sample, the fields of the phase transition lines (symbols) in Fig. 1*B* were slightly rescaled (*SI Appendix*, section S1). (*B*) Temperature-dependent electrical resistivity for selected magnetic fields $B = \mu_0 H \| [0\,0\,1]$. Curves with fields above 1.5 T are successively shifted downward by 3 μΩcm for better readability. The arrows indicate the temperatures down to which linear-in-T behavior is observed, suggesting a critical field close to 1.73 T. (*C*) Thermal expansion coefficient (left) and specific heat coefficient (right) vs. temperature near the respective critical fields B_Q (which are close to 1.95 T for the thermal expansion sample and 1.75 T for the specific heat sample [*SI Appendix*, section S1]). (*D*) A coefficient of the FL part (main text) of the electrical resistivity vs. applied magnetic field $B = \mu_0 H$. The error bars represent standard deviations of the fit. *Inset* expands the field range around B_Q, revealing the divergence of A. Lines are guides to the eyes.

plot (Fig. 3*G*); it extrapolates to infinite sharpness in the zero-temperature limit and thus a jump in the Fermi surface. The power is 1 within error bars (Fig. 3 legend) for both the magnetoresistance and the Hall cross-over at B_Q, similar to what was previously found for the quantum critical point (QCP) at the border of the AFM phase in both $Ce_3Pd_{20}Si_6$ (15) and $YbRh_2Si_2$ (10, 14). Note that, in the low-temperature limit, the change Δn in the effective charge carrier concentration across B_Q, estimated using a simple spherical Fermi-surface 1-band approach, is sizeable: It is about 0.35 electrons per Ce atom at the $8c$ site (Fig. 3*H*).

While a change in Fermi surface per se could come from a Lifshitz transition, our observations near B_Q (and B_N) are very different. Lifshitz transitions for 3D Fermi surfaces, as observed in the high-field regime of $YbRh_2Si_2$ (31), take place in the Fermi-liquid part of the phase diagram (32) and give rise to only smooth evolutions of the Hall coefficient. Instead, strange-metal behavior accompanied by a sizeable jump of the Fermi surface is the hallmark of unconventional quantum criticality driven by Kondo destruction. The question, then, is how multiple stages of Kondo destruction may arise under the tuning of a single control parameter. We consider a multipolar Kondo model that contains a lattice of local moments with a 4-fold degeneracy (classified as Γ_8 by the crystalline point group symmetry; *SI Appendix*, section S4), whose spin and orbital states are described by $\boldsymbol{\sigma}$ and $\boldsymbol{\tau}$, respectively, and conduction electrons, $c_{\mathbf{k}\sigma\tau}$, as sketched in Fig. 4*D*. The Γ_8 moments are Kondo coupled to the conduction electrons, and the coupling constants J_K^κ with $\kappa = \sigma, \tau, m$, respectively, describe the interaction of $\boldsymbol{\sigma}$, $\boldsymbol{\tau}$, and $\boldsymbol{\sigma} \otimes \boldsymbol{\tau}$ with the conduction-electron counterparts. The local moments also interact with each other by the RKKY exchange interactions I_{ij}^κ between sites i and j which, for the purpose of computational feasibility, we have chosen to be of Ising type (*SI Appendix*, section S5). In the extended dynamical mean-field theory (*SI Appendix*, section S5), this will be described in terms of the coupling between the local moments and bosonic baths ϕ_κ, with coupling constants g_κ. We are then led to analyze the multipolar Bose–Fermi Kondo (BFK) model as an effective model for the Kondo lattice, which is described by the Hamiltonian (see *SI Appendix*, section S5 for more details)

$$H_{\mathrm{BFK}} = H_{\mathrm{K}} + H_{\mathrm{BK}} + H_{\mathrm{B0}}(\phi_\sigma, \phi_\tau, \phi_m), \qquad [1]$$

with $H_{\mathrm{BK}} = g_\sigma\, \sigma^z\, \phi_\sigma + g_\tau\, \tau^z\, \phi_\tau + g_m\, (\sigma^z \otimes \tau^z)\, \phi_m$. Here, H_{K} describes the Kondo coupling between the local spin–orbital moments and the conduction electrons. In addition, H_{BK} expresses the Bose–Kondo coupling between the local moments and the bosonic baths whose dynamics are specified by H_{B0}. For the pure (fermionic) Kondo part, our model corresponds to an exactly screened Kondo problem (33), and is SU(4) symmetric when J_K^κ is the same for $\kappa = \sigma, \tau, m$. Even when the SU(4) symmetry is broken, the system flows to the exactly screened (Fermi liquid) SU(4) Kondo fixed point (34, 35). The model in the presence of bosonic Kondo couplings has not been studied before. Based on what is known for the SU(2) Bose–Fermi Kondo model (36, 37), we expect that the overall phase diagram of the present model with different kinds of symmetries in the SU(4) space is captured by the calculations with SU(4)-symmetric Kondo couplings and Ising-anisotropic bosonic couplings (*SI Appendix*, section S4). We have determined the zero-temperature phase

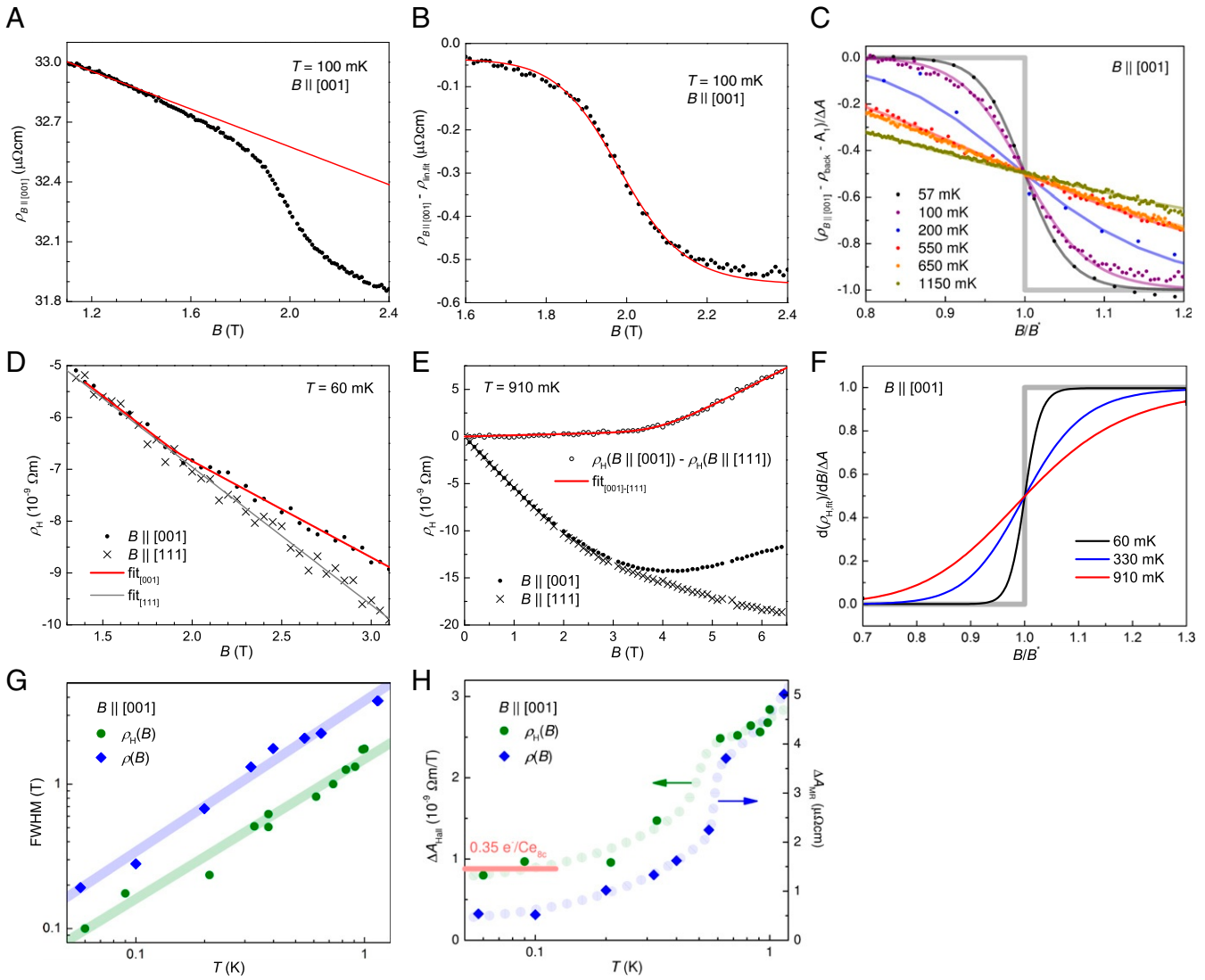

Fig. 3. Magnetotransport isotherms across the QCP at the border of the AFQ phase in $Ce_3Pd_{20}Si_6$. (*A*) Electrical resistivity vs. magnetic field at 100 mK. The solid red line represents a linear background contribution. (*B*) Difference of electrical resistivity and the background fit of *A*. The solid red line represents a phenomenological cross-over fit (*SI Appendix*, section S3). (*C*) Selected scaled magnetoresistance isotherms vs. scaled magnetic field (data points), together with the cross-over fits (solid lines). An extended field range is shown in *SI Appendix*, Fig. S3. (*D*) Hall resistivity vs. magnetic field at 60 mK, for 2 different field directions. The solid gray line represents a fit to the data for fields along [1 1 1] for which no quantum criticality exists near 2 T (28, 30) and for which ρ_H is simply linear in *B*. The solid red line is a cross-over fit (*SI Appendix*, section S3) to the data for fields along [0 0 1]. Its low-field slope is fixed to the slope of the data for fields along [1 1 1]. The full field range is shown in *SI Appendix*, Fig. S4. (*E*) $\rho_H(B)$ data at 910 mK. Subtraction of the data for the field along [1 1 1] singles out the contribution due to the QCP at B_Q in the $\rho_H(B\|[0\,0\,1])$ data. (*F*) Selected scaled derivatives of the Hall resistivity cross-over fits with respect to field vs. scaled magnetic field. (*G*) FWHM of the cross-overs in magnetoresistance in *C* and the Hall resistivity derivatives in *F*. The straight lines are best fits to FHWM $\propto T^a$, with $a = 1.05 \pm 0.05$ and 0.97 ± 0.05 for the magnetoresistance and Hall cross-over, respectively (*SI Appendix*, Fig. S5). (*H*) Step heights of the magnetoresistance and Hall resistance cross-overs. Indicated in red is the effective charge carrier concentration change, estimated using a spherical Fermi-surface 1-band approach. The thick gray lines in *C* and *F* correspond to extrapolations to $T = 0$, where according to the FWHM the cross-overs are sharp steps ("jumps").

diagram of this SU(4)-based Bose–Fermi Kondo model via calculations using a continuous-time quantum Monte Carlo method (*SI Appendix*, section S5).

The theoretical phase diagram is illustrated in Fig. 4*B*, as a function of $g_1 = g_\tau + g_\sigma$ and $g_2 = g_\tau - g_\sigma$, for fixed non-zero values of g_m and J_K^κ. Consider a generic direction (cut δ). In phase "σ, τ Kondo," both the spin and orbital moments are Kondo entangled, which gives rise to an SU(4)-symmetric electron fluid (Fig. 4 *C* and *E*, *Right*). Upon moving toward the left (against the direction of arrow δ), this state first undergoes the destruction of the Kondo effect in the orbital sector at one QCP (stars in Fig. 4 *B* and *C*). This drives the system into a phase in which only the spin moments form a Kondo singlet with the conduction electrons (phase "σ Kondo, τ KD" in Fig. 4 *B* and *C* and *E*, *Left*). It then, at the next QCP (squares in Fig. 4 *B* and *C*), experiences the destruction of the Kondo effect in the spin sector, leading to a fully Kondo destroyed state (phase "σ, τ KD" in Fig. 4 *B* and *C*). Consequently, in a multipolar Kondo lattice system, there will be 2 distinct QCPs associated with a sequence of Kondo destructions. At each of the QCPs, the Fermi surface undergoes a sudden reconstruction (circles in Fig. 4*C*), which explains the jumps inferred from the Hall coefficient and magnetoresistance data. For a single-band jellium-like electronic fluid, our theory implies an integer jump of the electron count

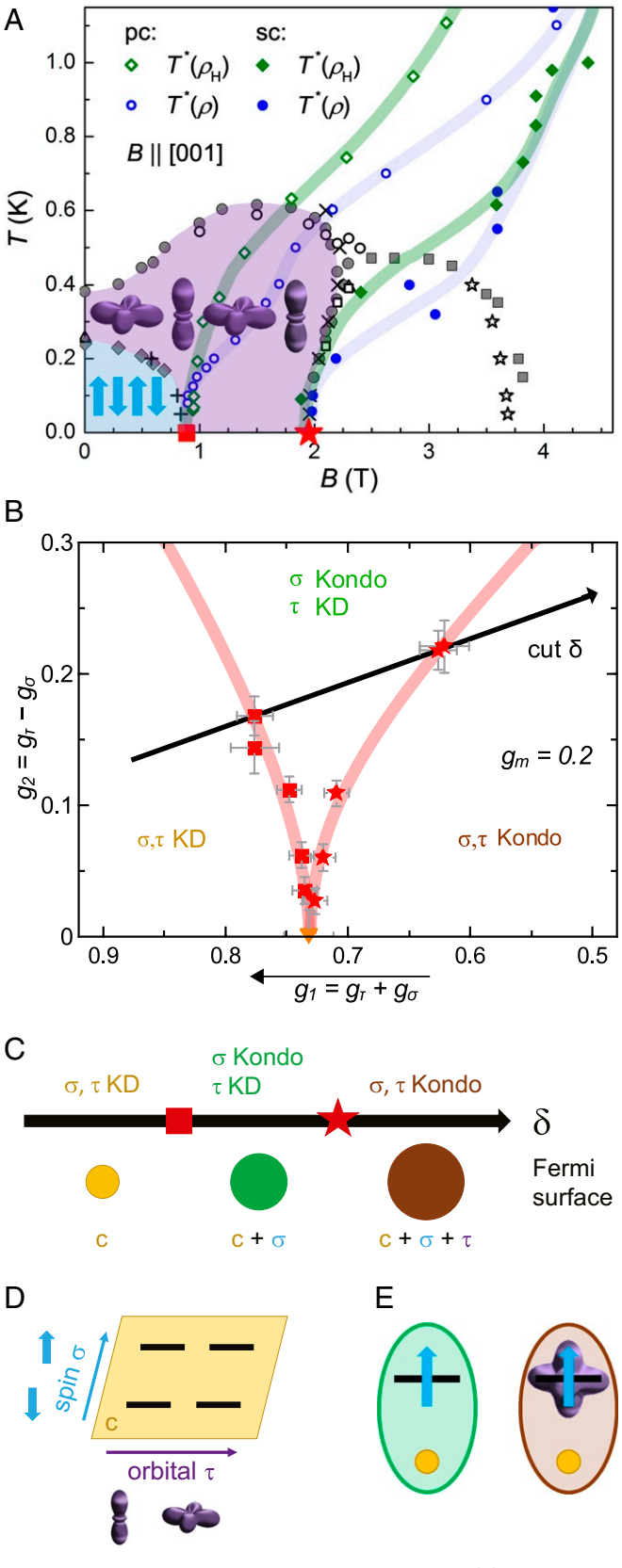

Fig. 4. Two-stage Kondo destruction in $Ce_3Pd_{20}Si_6$. (*A*) Experimental temperature–magnetic-field phase diagram from Fig. 1*B*, with T^* scales across which the Kondo entanglement in the spin and orbital channel breaks up at 2 consecutive QCPs, marked by the red square (at B_N) and the red star (at B_Q), respectively. The T^* scales at B_N are taken from Hall resistivity [$T^*(\rho_H)$] and the magnetoresistance [($T^*(\rho)$] measurements on a polycrystal (pc) (15). The corresponding T^* scales at B_Q, extracted from the magnetotransport cross-overs in Fig. 3 for our transport single crystal (sc), were slightly rescaled in B to match the higher critical field of the single crystals defining the phase boundaries (*SI Appendix*, section S1). The shaded regions with the spin and orbital symbols visualize the AFM and AFQ phases, respectively. (*B*) Theoretical phase diagram (at $T = 0$) of the BFK model in the $g_1 - g_2$ plane. Red squares and stars mark the spin and orbital Kondo destruction QCPs, respectively. The thick black arrow represents a generic trajectory in the parameter space. The orange triangle represents the special case $g_2 = 0$, where $g_\tau = g_\sigma$ and the 2 transitions occur simultaneously. (*C*) Schematic of the sequential Kondo destruction transitions, from a phase with Kondo destruction (KD) in both the spin (σ) and orbital (τ) channels, via a phase where only the spin is Kondo screened, to a phase with full Kondo screening. (*D*) Schematic of the 4-fold degeneracy of the Γ_8 ground state. (*E*) Sketches of the Kondo entangled states with spin-only (*Left*) and full Kondo entanglement (*Right*). The horizontal bars represent local degrees of freedom and the yellow plane and circles the conduction electrons.

at each QCP. Any real material would, however, show deviations from this equality, as also seen here (above). The precise statement is that a jump in the electron count and Fermi surfaces must be manifested in the extrapolated zero-temperature limit of the Hall cross-over, as we have demonstrated. We stress that an applied magnetic field is expected to weaken magnetic order more rapidly ($\sim B$) than the Kondo processes ($\sim B^2$); related considerations apply to the quadrupolar sector. Thus, the sequential Kondo destruction happens upon decreasing the magnetic field, i.e., from right to left in the experimental phase diagram (Fig. 4*A*).

We have thus demonstrated that, despite the genuine intermixing of the 2 degrees of freedom in the many-body dynamics, a remarkable separation of their fingerprints occurs in the singular physics of quantum criticality: The magnetic-field tuning realizes 2 stages of quantum phase transitions, which are respectively dictated by the Kondo destruction of the spin and orbital sectors.

Discussion

To put this finding in perspective, we recall that in spin-only systems, experiments have provided extensive evidence for Kondo destruction in AFM heavy fermion compounds (9, 10, 14, 15, 38, 39). From studying a spin–orbital heavy fermion system, we have shown that Kondo destruction is a general phenomenon and may also occur if degrees of freedom other than spin decouple from the conduction electrons. This demonstrates Kondo destruction as a general framework for both beyond-Landau quantum criticality and the electron localization–delocalization transition in metallic heavy fermion systems. Our analysis of the multipolar degrees of freedom also relates to the purely orbital case, as realized for instance in the Pr-based heavy fermion systems PrV_2Al_{20} (40) and $PrIr_2Zn_{20}$ (41). These materials show unusual multipolar quantum criticality, although Kondo destruction has not yet been explored. Future studies may reveal whether electron localization occurs in these orbital-only heavy fermion systems as well and contributes to nucleating phases (42, 43)—including unconventional superconductivity (44, 45).

More generally, we have demonstrated that strange-metal properties occur at each stage of the electron localization transition. This finding connects well with other classes of strongly correlated systems in which strange-metal behavior has also been linked to electron localization. In the high-T_c cuprate superconductors, electron localization as suggested by a pronounced change of the Fermi surface (4, 7) and a divergence of the charge carrier mass (5) appears near the hole doping for optimal superconductivity, where strange-metal properties arise. In organic systems, electron localization has also been evidenced in connection with strange-metal behavior and optimal

superconductivity (12). In the graphene superlattices with a magic-angle twist, whose electronic states may also satisfy an SU(4) symmetry from the combination of the spin and valley degrees of freedom, transport and quantum oscillation measurements (6) have implicated a "small" Fermi surface of the charge carriers doped into a Mott insulator, thereby raising the possibility of an electron localization–delocalization transition underlying the superconductivity. As such, our work sheds light on the breakdown of the textbook description of electrons in solids and points to electron localization as a robust organizing principle for strange-metal behavior and, by extension, high-temperature superconductivity.

Our system contains strongly correlated and entwined degrees of freedom; the crystalline symmetry dictates the strong intermixing of the spin and orbital quantum numbers. Yet, near each of the 2 QCPs, there is a clear selection of the orbital or spin channel that drives the quantum critical singularity. This remarkable simplicity, developed out of the intricate interplay among the multiple degrees of freedom, elucidates the physics of complex electron fluids. This understanding may also impact strongly correlated systems beyond the realm of materials such as mesoscopic structures (46) and quantum atomic fluids (47, 48), where localization–delocalization transitions may also play an important role. Finally, the sequential localization we have advanced may be viewed as selectively coupling only part of the system to an environment. This notion relates to ideas for reduced dephasing within a logical subspace (49) and may as such inspire additional settings for quantum technology.

Materials and Methods

Materials and methods are described in *SI Appendix*.

ACKNOWLEDGMENTS. We thank D. Joshi for his contribution to the crystal growth; R. Dumas from Quantum Design for contributing to the heat capacity measurements; T. Sakakibara for sharing data of ref. 30 with us; L. Bühler for graphical design; and E. Abrahams, S. Kirchner, D. Natelson, A. Nevidomskyy, T. Park, and S. Wirth for fruitful discussions. The work in Vienna was funded by the Austrian Science Fund (P29296-N27 and DK W1243), the European Research Council (Advanced Grant 227378), and the US Army Research Office (ARO-W911NF-14-1-0496). The work at Rice University was in part supported by the National Science Foundation (NSF) (DMR-1920740) and the Robert A. Welch Foundation (C-1411) (to A.C., E.M.N., C.-C.L., and Q.S.), the Army Research Office (W911NF-14-1-0525) and a Smalley Postdoctoral Fellowship at the Rice Center for Quantum Materials (to H.-H.L.), and the Big-Data Private-Cloud Research Cyberinfrastructure MRI Award funded by the NSF (CNS-1338099) and by an IBM Shared University Research Award. V.M. was supported by the Fundação Carlos Chagas Filho de Amparo à Pesquisa do Estado do Rio de Janeiro (201.755/2015), R.Y. by the National Science Foundation of China (11674392) and the Ministry of Science and Technology of China (National Program on Key Research, 2016YFA0300504), K.I. by the NSF (Grant DMR-1508122), and A.M.S. by the South African National Research Foundation (93549) and the University of Johannesburg Faculty Research Committee/University Research Committee. Q.S. acknowledges the hospitality of the Aspen Center for Physics (NSF, PHY-1607611) and University of California, Berkeley.

1. Y. Tokura, N. Nagaosa, Orbital physics in transition-metal oxides. *Science* **288**, 462–468 (2000).
2. Q. Si, R. Yu, E. Abrahams, High-temperature superconductivity in iron pnictides and chalcogenides. *Nat. Rev. Mater.* **1**, 16017 (2016).
3. Y. Takabayashi *et al.*, The disorder-free non-BCS superconductor Cs3C60 emerges from an antiferromagnetic insulator parent state. *Science* **323**, 1585–1590 (2009).
4. S. Badoux *et al.*, Change of carrier density at the pseudogap critical point of a cuprate superconductor. *Nature* **531**, 210–214 (2016).
5. B. J. Ramshaw *et al.*, Quasiparticle mass enhancement approaching optimal doping in a high-T_c superconductor. *Science* **348**, 317–320 (2015).
6. Y. Cao *et al.*, Unconventional superconductivity in magic-angle graphene superlattices. *Nature* **556**, 43–50 (2018).
7. F. F. Balakirev *et al.*, Signature of optimal doping in Hall-effect measurements on a high-temperature superconductor. *Nature* **424**, 912–915 (2003).
8. T. Park *et al.*, Isotropic quantum scattering and unconventional superconductivity. *Nature* **456**, 366–368 (2008).
9. A. Schröder *et al.*, Onset of antiferromagnetism in heavy-fermion metals. *Nature* **407**, 351–355 (2000).
10. S. Paschen *et al.*, Hall-effect evolution across a heavy-fermion quantum critical point. *Nature* **432**, 881–885 (2004).
11. E. Schuberth *et al.*, Emergence of superconductivity in the canonical heavy-electron metal $YbRh_2Si_2$. *Science* **351**, 485–488 (2016).
12. H. Oike, K. Miyagawa, H. Taniguchi, K. Kanoda, Pressure-induced Mott transition in an organic superconductor with a finite doping level. *Phys. Rev. Lett.* **114**, 067002 (2015).
13. Q. Si, S. Paschen, Quantum phase transitions in heavy fermion metals and Kondo insulators. *Phys. Status Solidi B* **250**, 425–438 (2013).
14. S. Friedemann *et al.*, Fermi-surface collapse and dynamical scaling near a quantum-critical point. *Proc. Natl. Acad. Sci. U.S.A.* **107**, 14547–14551 (2010).
15. J. Custers *et al.*, Destruction of the Kondo effect in the cubic heavy-fermion compound $Ce_3Pd_{20}Si_6$. *Nat. Mater.* **11**, 189–194 (2012).
16. Y. Luo *et al.*, Heavy-fermion quantum criticality and destruction of the Kondo effect in a nickel-oxypnictide. *Nat. Mater.* **13**, 777–781 (2014).
17. L. S. Wu *et al.*, Orbital-exchange and fractional quantum number excitations in an f-electron metal, Yb_2Pt_2Pb. *Science* **352**, 1206–1210 (2016).
18. L. Prochaska *et al.*, Singular charge fluctuations at a magnetic quantum critical point. arXiv:1808.02296 (7 August 2018).
19. Q. Si, S. Rabello, K. Ingersent, J. Smith, Locally critical quantum phase transitions in strongly correlated metals. *Nature* **413**, 804–808 (2001).
20. P. Coleman, C. Pépin, Q. Si, R. Ramazashvili, How do Fermi liquids get heavy and die? *J. Phys. Condens. Matter* **13**, R723–R738 (2001).
21. T. Senthil, M. Vojta, S. Sachdev, Weak magnetism and non-Fermi liquids near heavy-fermion critical points. *Phys. Rev. B* **69**, 035111 (2004).
22. A. Cai, H. Hu, K. Ingersent, S. Paschen, Q. Si, Dynamical Kondo effect and Kondo destruction in effective models for quantum critical heavy fermion metals. arXiv:1904.11471 (25 April 2019).
23. R. Shiina, H. Shiba, P. Thalmeier, Magnetic-field effects on quadrupolar ordering in a Γ_8-quartet system CeB_6. *J. Phys. Soc. Jpn.* **66**, 1741–1755 (1997).
24. P. Y. Portnichenko *et al.*, Incommensurate short-range multipolar order parameter of phase II in $Ce_3Pd_{20}Si_6$. *Phys. Rev. B* **94**, 245132 (2016).
25. A. V. Gribanov, Y. D. Seropegin, O. I. Bodak, Crystal structure of the compounds $Ce_3Pd_{20}Ge_6$ and $Ce_3Pd_{20}Si_6$. *J. Alloys Comp.* **204**, L9–L11 (1994).
26. A. Prokofiev *et al.*, Crystal growth and composition-property relationship of $Ce_3Pd_{20}Si_6$ single crystals. *Phys. Rev. B* **80**, 235107 (2009).
27. P. P. Deen *et al.*, Quantum fluctuations and the magnetic ground state of $Ce_3Pd_{20}Si_6$. *Phys. Rev. B* **81**, 064427 (2010).
28. H. Ono *et al.*, Magnetic phase diagram of clathrate compound $Ce_3Pd_{20}Si_6$ with quadrupolar ordering. *J. Phys. Condens. Matter* **25**, 126003 (2013).
29. G. R. Stewart, Non-Fermi-liquid behavior in *d*- and *f*-electron metals. *Rev. Mod. Phys.* **73**, 797–855 (2001).
30. H. Mitamura *et al.*, Low temperature magnetic properties of $Ce_3Pd_{20}Si_6$. *J. Phys. Soc. Jpn.* **79**, 074712 (2010).
31. H. Pfau *et al.*, Interplay between Kondo suppression and Lifshitz transitions in $YbRh_2Si_2$ at high magnetic fields. *Phys. Rev. Lett.* **110**, 256403 (2013).
32. P. Gegenwart *et al.*, High-field phase diagram of the heavy-fermion metal $YbRh_2Si2$. *New J. Phys.* **8**, 171 (2006).
33. A. C. Hewson, *The Kondo Problem to Heavy Fermions* (Cambridge University Press, Cambridge, UK, 1997).
34. H. Pang, Non-Fermi-liquid states in a generalized two-channel Kondo model. *Phys. Rev. Lett.* **73**, 2736–2739 (1994).
35. K. Le Hur, P. Simon, L. Borda, Maximized orbital and spin Kondo effects in a single-electron transistor. *Phys. Rev. B* **69**, 045326 (2004).
36. L. Zhu, Q. Si, Critical local-moment fluctuations in the Bose-Fermi Kondo model. *Phys. Rev. B* **66**, 024426 (2002).
37. G. Zaránd, E. Demler, Quantum phase transitions in the Bose-Fermi Kondo model. *Phys. Rev. B* **66**, 024427 (2002).
38. H. Shishido, R. Settai, H. Harima, Y. Onuki, A drastic change of the Fermi surface at a critical pressure in $CeRhIn_5$: dHvA study under pressure. *J. Phys. Soc. Jpn.* **74**, 1103–1106 (2005).
39. E. D. Mun *et al.*, Magnetic-field-tuned quantum criticality of the heavy-fermion system YbPtBi. *Phys. Rev. B* **87**, 075120 (2013).
40. Y. Shimura *et al.*, Field-induced quadrupolar quantum criticality in PrV_2Al_{20}. *Phys. Rev. B* **91**, 241102 (2015).
41. T. Onimaru *et al.*, Quadrupole-driven non-Fermi-liquid and magnetic-field-induced heavy fermion states in a non-Kramers doublet system. *Phys. Rev. B* **94**, 075134 (2016).
42. J. A. Mydosh, P. M. Oppeneer, Colloquium: Hidden order, superconductivity, and magnetism: The unsolved case of URu_2Si_2. *Rev. Mod. Phys.* **83**, 1301–1322 (2011).
43. A. McCollam, B. Andraka, S. R. Julian, Fermi volume as a probe of hidden order. *Phys. Rev. B* **88**, 075102 (2013).
44. E. D. Bauer, N. A. Frederick, P. C. Ho, V. S. Zapf, M. B. Maple, Superconductivity and heavy fermion behavior in $PrOs_4Sb_{12}$. *Phys. Rev. B* **65**, 100506 (2002).
45. K. Matsubayashi *et al.*, Pressure-induced heavy fermion superconductivity in the nonmagnetic quadrupolar system $PrTi_2Al_{20}$. *Phys. Rev. Lett.* **109**, 187004 (2012).
46. A. J. Keller *et al.*, Emergent SU(4) Kondo physics in a spin-charge-entangled double quantum dot. *Nat. Phys.* **10**, 145–150 (2014).
47. S. Nakamura, K. Matsui, T. Matsui, H. Fukuyama, Possible quantum liquid crystal phases of helium monolayers. *Phys. Rev. B* **94**, 180501 (2016).
48. M. Neumann, J. Nyeki, B. Cowan, J. Saunders, Bilayer ^{3}He: A simple two-dimensional heavy-fermion system with quantum criticality. *Science* **317**, 1356–1359 (2007).
49. M. Friesen, J. Ghosh, M. A. Eriksson, S. N. Coppersmith, A decoherence-free subspace in a charge quadrupole qubit. *Nat. Commun.* **8**, 15923 (2017).